

Wannier center sheets in topological insulators

Maryam Taherinejad,^{*} Kevin F. Garrity, and David Vanderbilt

Department of Physics and Astronomy, Rutgers University, Piscataway, New Jersey 08854-0849, USA

(Received 20 December 2013; revised manuscript received 19 February 2014; published 3 March 2014)

We argue that various kinds of topological insulators (TIs) can be insightfully characterized by an inspection of the charge centers of the hybrid Wannier functions, defined as the orbitals obtained by carrying out a Wannier transform on the Bloch functions in one dimension while leaving them Bloch-like in the other two. From this procedure, one can obtain the Wannier charge centers (WCCs) and plot them in the two-dimensional projected Brillouin zone. We show that these WCC sheets contain the same kind of topological information as is carried in the surface energy bands, with the crucial advantage that the topological properties of the bulk can be deduced from bulk calculations alone. The distinct topological behaviors of these WCC sheets in trivial, Chern, weak, strong, and crystalline TIs are first illustrated by calculating them for simple tight-binding models. We then present the results of first-principles calculations of the WCC sheets in the trivial insulator Sb_2Se_3 , the weak TI KHgSb , and the strong TI Bi_2Se_3 , confirming the ability of this approach to distinguish between different topological behaviors in an advantageous way.

DOI: [10.1103/PhysRevB.89.115102](https://doi.org/10.1103/PhysRevB.89.115102)

PACS number(s): 71.90.+q, 72.25.-b, 73.20.At, 73.43.-f

I. INTRODUCTION

Since the work of Thouless *et al.* [1] relating the Chern number to the integer quantum Hall effect, there has been great interest in insulators with topologically nontrivial band structures. In time-reversal-invariant insulators, the first Chern number vanishes, but topologically nontrivial band structures can still emerge in systems with strong spin-orbit coupling [2–5] or crystal point-group symmetries [6]. These topological phases are classified by a series of Z_2 invariants. In two dimensions, a single Z_2 invariant distinguishes a quantum spin Hall system from a trivial two-dimensional (2D) insulator, while in three dimensions (3D), a total of four Z_2 invariants [$\nu_0, \nu_1, \nu_2, \nu_3$] are needed to classify the trivial, weak, and strong topological phases which can emerge. The topologically nontrivial phases are gapped in the bulk, like trivial insulators, but by the bulk-edge correspondence they are required to have robust metallic states on the edge (2D) [7–10] or surface (3D) [11]. These surface states provide the strongest experimentally accessible signature of insulators with nontrivial topology [12–19]. However, for reasons of both computational efficiency and theoretical clarity, it is preferable to be able to calculate and understand the topological phases of insulators purely from bulk calculations.

There have been several previously proposed methods for calculating Z_2 invariants. In principle, it is possible to calculate them by integrating the Berry connection on half of the Brillouin zone (BZ) [20], but this method requires fixing the gauge of the wave functions, which is challenging in numerical calculations. In the special case of a centrosymmetric crystal, the Z_2 invariants can be calculated simply by considering the parity eigenvalues of the occupied electronic states at the time-reversal-invariant (TRI) momenta. The topological invariants of different phases can also be derived from the scattering matrix at the Fermi level [21]. Our current work is closely related to a recently developed method which is both general (not limited to crystals with special symmetries) and

computationally efficient [22–25]. This method relies on the use of hybrid Wannier functions (WFs), which provide an alternative to the Bloch representation of the occupied band subspace. By following the evolution of hybrid WFs around a closed loop in the BZ, we can describe the adiabatic, unitary evolution of the occupied Bloch bands. The partner switching of these Wannier charge centers (WCC) around a closed loop, which describes a pumping of “time-reversal polarization,” has been employed to calculate the Z_2 invariants in TRI insulators [22,23,26,27].

In this work, we focus on the topological properties of WCCs in 3D materials, which are functions of momentum k in two dimensions and can be plotted as sheets over the 2D BZ. Unlike the surface states, the behavior of these sheets is independent of surface termination and depends purely on the bulk wave functions. We explain why a bulk-edge correspondence between the surface energy bands and bulk WCCs is expected, and illustrate this correspondence in trivial, Chern, weak topological, strong topological, and crystalline topological insulators (TIs) using tight-binding models and first-principles calculations. Although a knowledge of the behavior of the WCCs on certain 2D planes in the 3D k space is sufficient to determine the topological phase in some cases, as for 3D TRI insulators, the more general behavior of the WCC sheets in different topological phases, including the crystalline topological phase, can provide new insights into the origin and properties of these phases. In addition, the pure bulk origin of their characterization allows for a simpler picture of many properties.

The paper is organized as follows. In Sec. II, we define the WCC sheets, explain how to construct them, consider their symmetry properties, and discuss the bulk-boundary correspondence that relates the bulk WCCs to the surface energy bands. In Sec. III, we introduce the tight-binding models that will be used for illustrative calculations. We also present the materials systems that will be the subject of first-principles calculations, and discuss the details of the computational methods. The calculated WCC sheets are presented and discussed in Sec. IV, and we end with a summary in Sec. V.

^{*}mtaheri@physics.rutgers.edu

II. WCC SHEETS

The electronic ground state in periodic crystalline solids is naturally described by extended Bloch functions $|\psi_{n\mathbf{k}}\rangle$, or the cell-periodic versions $|u_{n\mathbf{k}}\rangle = e^{-i\mathbf{k}\cdot\mathbf{r}}|\psi_{n\mathbf{k}}\rangle$, labeled by the band n and crystal momentum \mathbf{k} . An alternative representation is the set of localized orbitals or Wannier functions (WF) which are defined in relation to the Bloch functions by a unitary transformation:

$$|W_n(\mathbf{R})\rangle = \frac{1}{(2\pi)^3} \int_{\text{BZ}} d\mathbf{k} e^{i\mathbf{k}\cdot(\mathbf{r}-\mathbf{R})} |u_{n\mathbf{k}}\rangle. \quad (1)$$

These WFs are not unique, as the $U(N)$ gauge freedom in choosing the N representatives of the occupied space at each \mathbf{k} point $|\tilde{u}_{n\mathbf{k}}\rangle = \sum_m U_{mn}(\mathbf{k})|u_{m\mathbf{k}}\rangle$ leaves them gauge dependent.

In one dimension (1D), there is a unique gauge that minimizes the spread functional of the WFs [28]. These maximally localized WFs are eigenfunctions of the band-projected position operator PzP , where $P = \sum_{n\mathbf{k}} |\psi_{n\mathbf{k}}\rangle\langle\psi_{n\mathbf{k}}|$ is the projection operator onto the occupied bands. In 2D and 3D, on the other hand, the WFs can not be maximally localized in all directions simultaneously because the operators PxP , PyP , and PzP do not commute and it is not possible to choose the WFs to be simultaneous eigenfunctions of all three. Instead, a compromise can be achieved through an iterative procedure that localizes the WFs in all directions as much as possible [28].

Insulators for which the occupied bands are characterized by a nonzero Chern number are known as ‘‘Chern’’ or ‘‘quantum anomalous Hall’’ (QAH) insulators. In this case, it is well known that there is a topological obstruction to the construction of exponentially localized WFs [29,30]. The vanishing of the Chern number in TRI insulators guarantees the existence of localized WFs, but special care needs to be taken in choosing the gauge for Z_2 -odd insulators, as the localized WFs can only be constructed in a gauge which does not let them come in time-reversal pairs [31].

The fact that there is never a topological obstruction to the construction of WFs in 1D suggests that a convenient strategy for higher dimensions may be to construct ‘‘hybrid WFs’’ that are Wannier-like in 1D and Bloch-like in the remaining dimensions [28,32]. Choosing the \hat{z} direction for Wannierization in 3D, these take the form

$$|W_{nl_z}(k_x, k_y)\rangle = \frac{1}{2\pi} \int dk_z e^{i\mathbf{k}\cdot(\mathbf{r}-l_z c \hat{z})} |u_{n,\mathbf{k}}\rangle, \quad (2)$$

where l_z is a layer index and c is the lattice constant along \hat{z} . Since there is a unique construction of maximally localized WFs in 1D, these are easily constructed at each (k_x, k_y) , regardless of whether the system is a normal insulator or a Chern, Z_2 , crystalline, or any other kind of TI. The charge center of these hybrid WFs along the localized direction \bar{z}_n is defined as the expectation value $\bar{z}_n(k_x, k_y) = \langle W_{n0} | \hat{z} | W_{n0} \rangle$ of the position operator \hat{z} along this direction for the WF in the home unit cell $\mathbf{R} = 0$. These WCCs, which are eigenvalues of the PzP operator, have been useful in defining polarization in 2D Chern insulators [33], understanding polarization in 3D layered insulators [34], and calculating the Z_2 topological invariants in TRI insulators [22]. Their sum over occupied bands also gives the ‘‘polarization structure’’ describing the Berry-phase contribution to the electric polarization as a function of \mathbf{k} in the 2D BZ [35].

It is well known that the nontrivial topology of Chern, Z_2 , and crystalline TIs is reflected in a corresponding nontrivial connectivity of the surface energy bands. While k_z is clearly no longer a good quantum number for a surface normal to \hat{z} , k_x and k_y are still conserved, so that if surface states appear in the bulk energy gap, their energy dispersions $\epsilon_n(k_x, k_y)$ are good functions of momenta in the surface BZ. In a similar way, the WCCs $\bar{z}_n(k_x, k_y)$ can be plotted over the same 2D BZ, where the Wannierized real-space direction plays a role analogous to the surface normal. Unlike the surface states $\epsilon_n(k_x, k_y)$, the WCCs $\bar{z}_n(k_x, k_y)$ depend only on bulk properties. However, they still carry the same kind of topological information as is contained in the surface states, as will be explained in Sec. II B. The WCCs can be obtained from a parallel-transport-based construction [28,34] in a straightforward way, as explained next.

A. Construction

A cell-periodic Bloch state $|u_{\mathbf{k}}\rangle$ belonging to an isolated band can be parallel transported to $|u_{\mathbf{k}+\mathbf{b}}\rangle$ by choosing the phase of the latter such that the overlap $\langle u_{\mathbf{k}} | u_{\mathbf{k}+\mathbf{b}} \rangle$ is real and positive, so that the change in the state is orthogonal to the state itself. If this is carried out repeatedly for a k -point string extending along the k_z direction by a reciprocal lattice vector $\mathbf{G} \parallel \hat{z}$, then once the phase of the initial $|u_{\mathbf{k}_0}\rangle$ is chosen, the phase of each subsequent state, including the final $|u_{\mathbf{k}_0+\mathbf{G}}\rangle$, is determined by this parallel-transport procedure. The phase of the last state on the string is then compared with the one $|\tilde{u}_{\mathbf{k}_0+\mathbf{G}}\rangle$ obtained by applying the periodic gauge condition $|\psi_{\mathbf{k}_0+\mathbf{G}}\rangle = |\psi_{\mathbf{k}_0}\rangle$, i.e., $\tilde{u}_{\mathbf{k}_0+\mathbf{G}}(\mathbf{r}) = \exp(-i\mathbf{G}\cdot\mathbf{r})u_{\mathbf{k}_0}(\mathbf{r})$, and the phase mismatch $U = \langle u_{\mathbf{k}_0+\mathbf{G}} | \tilde{u}_{\mathbf{k}_0+\mathbf{G}} \rangle$ is computed. For a k -point string at \mathbf{k}_\perp in the 2D BZ, this yields the Berry phase $\phi(\mathbf{k}_\perp) = -\text{Im} \ln U(\mathbf{k}_\perp)$ and the WCC $\bar{z}(\mathbf{k}_\perp) = (c/2\pi)\phi(\mathbf{k}_\perp)$, where c is the lattice constant along \hat{z} . If the parallel-transported states themselves are not needed, the same result can be obtained more straightforwardly by computing $\phi = -\text{Im} \ln \prod \langle u_{\mathbf{k}} | u_{\mathbf{k}+\mathbf{b}} \rangle$, where the product is carried out along the string and the phases are chosen arbitrarily except for the periodic gauge condition that fixes the phase of the first and last k points in relation to each other.

In the multiband case, where n occupied bands are treated as a group regardless of possible internal crossings or degeneracies, the corresponding ‘‘non-Abelian’’ Berry phases ϕ_n can be determined by generalizing this procedure in terms of $n \times n$ matrix operations. For each pair of neighboring points along the string, the matrix $M_{mn}^{(\mathbf{k}, \mathbf{k}+\mathbf{b})} = \langle u_{m\mathbf{k}} | u_{n,\mathbf{k}+\mathbf{b}} \rangle$ is computed and subjected to the singular value decomposition $M = V \Sigma W^\dagger$, where V and W are unitary and Σ is real and diagonal (typically, nearly unity). Again, the states at the end point $\mathbf{k}_0 + \mathbf{G}$ are predetermined by those at the start \mathbf{k}_0 by the periodic gauge condition. We can then identify $U^{(\mathbf{k}, \mathbf{k}+\mathbf{b})} = V W^\dagger$ as the unitary rotation from \mathbf{k} to $\mathbf{k} + \mathbf{b}$, and the global unitary rotation matrix $\Lambda(\mathbf{k}_\perp) = \prod U^{(\mathbf{k}, \mathbf{k}+\mathbf{b})}$ is constructed as the product of these along the string. Being unitary, its eigenvalues λ_n are unimodular, and we can identify the non-Abelian Berry phases (also known as Wilson loop eigenvalues) as $\phi_n(\mathbf{k}_\perp) = -\text{Im} \ln \lambda_n(\mathbf{k}_\perp)$. The WCCs are then just

$$\bar{z}_n(\mathbf{k}_\perp) = \frac{c}{2\pi} \phi_n(\mathbf{k}_\perp). \quad (3)$$

As discussed in Ref. [28], this procedure gives the centers of the maximally localized Wannier functions in 1D algebraically, without the need for any iterative localization procedure; we just repeat this procedure for each \mathbf{k}_\perp to construct the WCC sheets.

B. Symmetries and topology

A major theme of this work is to show how the WCC sheet structure $\bar{z}_n(\mathbf{k}_\perp)$ shares many qualitative features with the surface energy band structure $\epsilon_n(\mathbf{k}_\perp)$, a manifestation of the bulk-boundary correspondence which relates the boundary modes to the topological character of the bulk. The WCCs $\bar{z}_n(\mathbf{k}_\perp)$ have the crucial advantage that they can be used to deduce the topological properties of the bulk from bulk properties alone.

In this section, we show that the WCC sheet structure obeys all of the symmetries that are found in the surface energy band structure, and sometimes more. In particular, when TR is present, the Kramers degeneracies found at the 2D time-reversal-invariant momenta (TRIM) in the surface energy band structure also necessarily appear in the WCC sheet structure. We also demonstrate the bulk-boundary correspondence by sketching a physical argument as to why the topological connectedness of the WCC sheets mirrors that of the surface band structure, providing access to the topological indices in a similar way.

1. Symmetry

To review, we consider a crystalline insulator with \hat{z} taken along a primitive reciprocal lattice vector, and let k_\parallel and \mathbf{k}_\perp denote the wave vectors parallel and perpendicular to \hat{z} , respectively. We then consider the surface band structure $\epsilon_n(\mathbf{k}_\perp)$ for a 1×1 (unreconstructed) surface that has been cut normal to \hat{z} , where n labels energy eigenstates lying in the bulk projected band gap. We also consider the WCC sheets $\bar{z}_n(\mathbf{k}_\perp)$ constructed as detailed in Sec. II A, where n labels the sheets with $-c/2 \leq z \leq c/2$ in one unit cell along z . In both cases, \mathbf{k}_\perp resides in the same 2D surface BZ (both functions have the same periodicity in \mathbf{k}_\perp).

An element $S = \{G|\boldsymbol{\tau}\}$ of the full space group \mathcal{S} is composed of a generalized rotation G (possibly improper, and possibly containing TR) followed by a possible fractional translation $\boldsymbol{\tau}$ (in nonsymmorphic crystals), in addition to lattice translations; the full point group \mathcal{G} is composed of all of the G appearing in the space-group elements.

The symmetry of the WCC sheets is controlled by the reduced space group $\mathcal{S}_W \subseteq \mathcal{S}$ and the corresponding point group $\mathcal{G}_W \subseteq \mathcal{G}$ defined by restricting the list of G 's to those that map \hat{z} onto $\pm\hat{z}$. For such operations, let $G = K T_z G_\perp$ where G_\perp is the in-plane rotation (possibly improper), T_z is either the identity or the simple mirror M_z , and K is either the identity or TR. Then, a space-group element $\{G|\boldsymbol{\tau}\} \in \mathcal{S}_W$ must transform a hybrid Wannier function $W_n(\mathbf{k}_\perp)$ into another hybrid Wannier function $W_{n'}(\pm G\mathbf{k}_\perp)$, with the Wannier center transformed as

$$\bar{z}_{n'}(\pm G_\perp \mathbf{k}_\perp) = T_z \bar{z}_n(\mathbf{k}_\perp) + \tau_z, \quad (4)$$

where the minus sign applies if G contains TR.

The symmetry of the surface band structure $\epsilon_n(\mathbf{k}_\perp)$, on the other hand, is associated with the space group $\mathcal{S}_S \subseteq \mathcal{S}_W$ with the additional constraints that its elements do not reverse \hat{z} to $-\hat{z}$ and do not contain partial translations τ_z along \hat{z} . Then, for any element $G = K G_\perp$ in the corresponding point group \mathcal{G}_S we have that

$$\epsilon_n(\pm G_\perp \mathbf{k}_\perp) = \epsilon_n(\mathbf{k}_\perp), \quad (5)$$

where again the minus sign applies if TR is involved.

Since $\mathcal{G}_S \subseteq \mathcal{G}_W$, it follows from Eq. (4) that the WCC sheets also obey

$$\bar{z}_n(\pm G_\perp \mathbf{k}_\perp) = \bar{z}_n(\mathbf{k}_\perp) \quad (6)$$

for any $G \in \mathcal{G}_S$. Thus, the WCC sheets show at least as much symmetry as the surface band structure. If the space group contains symmetry elements that reverse the z axis, then there is an additional symmetry $\bar{z}_n(\pm G_\perp \mathbf{k}_\perp) = -\bar{z}_n(\mathbf{k}_\perp)$ associated with these elements, or if it contains glide or screw operations along \hat{z} , then also $\bar{z}_n(\pm G_\perp \mathbf{k}_\perp) = \bar{z}_n(\mathbf{k}_\perp) + \tau_z$. These additional WCC symmetries have no counterpart in the surface band structure.

Finally, we note that TR symmetry plays a similar role for the WCC sheets as for the surface energy band structure. Specifically, for any $G \in \mathcal{G}_S$, a Kramers degeneracy is enforced whenever $G_\perp \mathbf{k}_\perp = -\mathbf{k}_\perp$ (modulo a reciprocal lattice vector), due to the antiunitary nature of the TR operation. In particular, if TR by itself is a symmetry, then the WCC sheets and the surface energy bands are guaranteed to touch and form Kramers pairs at all of the TRIM. Additionally, if $C_2^z \otimes \text{TR}$ is a symmetry, then both the WCCs and surface energy bands are Kramers degenerate everywhere in the 2D BZ.

2. Topology

Just as the symmetries of the surface band structure are replicated in the WCC sheet structure, a similar principle applies to the topological properties. This will be amply illustrated by the examples to follow, but we give here a sketch of a general argument that this should be so.

For simplicity, consider first a 2D Chern insulator lying in the y - z plane with one occupied band carrying a Chern number $C = +1$. Then, the WCC $\bar{z}(k_y)$ undergoes a shift by c as k_y is adiabatically carried from $k_y = 0$ to $2\pi/b$ (assuming a rectangular $b \times c$ unit cell), as shown in Fig. 1(a). This means that one electron is adiabatically pumped by $c\hat{z}$ during one cycle of k_y around the 1D BZ. If the edge band structure remained gapped throughout the cycle, this would lead to a contradiction since by conservation of charge, one extra electron per surface unit cell would reside on the top edge at the end of the cycle. However, the starting and ending points are physically identical, so the edge charge must be the same. This paradox can only be avoided if there is a surface state that emerges from the valence band, rises throughout the gap, and disappears into the conduction band during one cycle, as shown in Fig. 1(b). In this case, the sudden loss of one electron that occurs when the surface band crosses the Fermi energy compensates for the gradual gain of one electron from the pumping, restoring charge conservation. In other words, we conclude that the edge band structure has a state crossing the

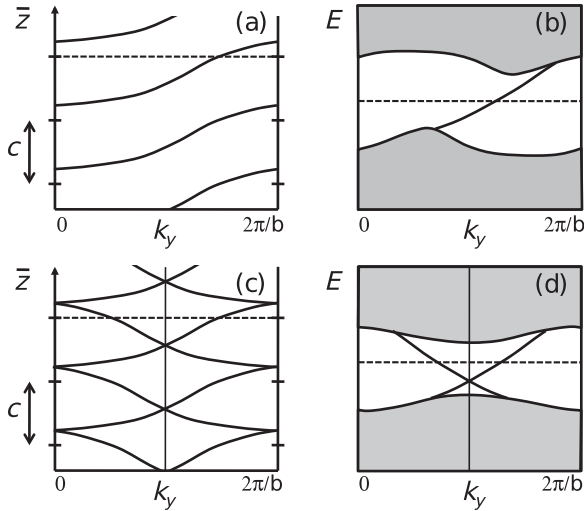


FIG. 1. (a) Flow of Wannier charge centers along \hat{z} vs k_y for a 2D Chern insulator. (b) Flow of surface energy bands vs k_y for a 2D Chern insulator. (c), (d) Same, but for a 2D Z_2 -odd (quantum spin Hall) insulator. Dashed lines are arbitrary reference positions in (a) and (c), or Fermi energies in (b) and (d).

gap if and only if the WCC structure has a WCC that winds by one unit during the cycle.

More generally, for an insulator with N occupied bands, if $\sum_n \bar{z}_n/c$ winds by Chern integer C during the cycle, the number of up-crossing minus the number of down-crossing surface bands in the edge band structure must equal C in order to satisfy charge conservation. The argument also generalizes to 3D Chern insulators. If the WCC sheet structure is computed in the \hat{z} direction, the Chern indices along x and y (that is, corresponding to Berry curvatures Ω_{yz} and $-\Omega_{xz}$) are evident in the z windings of the WCC sheets as \mathbf{k}_\perp is cycled in the k_y and k_x directions, respectively. In each case, a similar surface-state crossing necessarily must also occur in the surface band structure, following the arguments given above.

Turning now to TR-invariant insulators, the Chern number always vanishes, being odd under TR symmetry, but the WCC structure and surface band structure still share their topological properties. Recall that TR symmetry leads to double degeneracy in both the WCCs and the surface energy bands at TRI points in BZ. Here, we show that the WCCs connect the TRI points in the same manner as the energy bands do, and can be used in a similar way to deduce the Z_2 index of the system.

Consider the simple case of a 2D Z_2 insulator in the y - z plane with two occupied bands. The TR symmetry relates the WCCs and the surface energy bands in the second half of the BZ to those in the first half by $z(k_y) = z(2\pi/b - k_y)$ and $\epsilon(k_y) = \epsilon(2\pi/b - k_y)$, as illustrated in Figs. 1(c) and 1(d), so we only need to study their behavior in the first half $[0, \pi/b]$. In the absence of spin-mixing terms, the system decouples into two independent insulators with equal and opposite Chern numbers for spin-up and spin-down electrons. If these are ± 1 , the system is Z_2 odd. This implies both that the WCCs must switch partners as k_y evolves from 0 to π/c , as shown in Fig. 1(c), and that the surface energy bands zigzag, as shown

in Fig. 1(d). More precisely, an arbitrary horizontal line in Fig. 1(c) intersects the WCC curves just once (or, in general, an odd number of times) in the half-BZ, as does an arbitrary Fermi level in the half-BZ in Fig. 1(d). One unit of up spin, relative to down spin, is pumped to the edge during this half-BZ evolution, corresponding to the ‘‘TR polarization pumping’’ discussed by Fu and Kane [26]. For a Z_2 -even insulator, the number of crossings is, instead, an even integer (typically zero) for both the WCCs and the surface energy bands.

In more realistic Z_2 insulators, the spin-orbit interaction mixes up and down spins such that the energy bands are no longer perfectly spin polarized and a spin-Chern classification of the system is no longer guaranteed. However, as long as the bulk energy gap remains open as these spin-mixing terms are adiabatically turned on, neither the evenness/oddness of the number of WCC crossings, nor the evenness/oddness of the number of surface energy band crossings, can change. Therefore, it remains true that the Z_2 index deduced from the WCC evolution is the same as that deduced from the surface energy bands, i.e., they both contain the same topological information.

The weak and strong topological indices of a 3D TR-invariant insulator can be determined from the 2D indices on the six TRI faces $\tilde{k}_j = \{0, \pi\}$ of the 3D BZ (where $\tilde{k}_x = k_x a$, $\tilde{k}_y = k_y b$, $\tilde{k}_z = k_z c$), which are negative if the WCCs have a nontrivial connectedness on that face and positive otherwise. Assigning an index $\nu(\tilde{k}_i)$ to each of these faces, the four Z_2 invariants $[\nu_0, \nu_1, \nu_2, \nu_3]$ that uniquely specify the topological phase of a TR-invariant insulator can be determined from these $\nu(\tilde{k}_i)$ as follows. The three $\nu_i \equiv \nu(\tilde{k}_i = \pi)$, which are known as weak topological indexes, are determined from the WCC behavior on the $\tilde{k}_i = \pi$ faces, while the strong topological index $\nu_0 \equiv \nu(\tilde{k}_i = 0)\nu(\tilde{k}_i = \pi)$ is only negative if the topological indices of opposing TRI faces are opposite, i.e., if the WCCs on the $\tilde{k}_i = 0$ and $\tilde{k}_i = \pi$ faces have different behavior. The indices could similarly be deduced from the behavior of the surface energy bands. For both the WCC and surface problems, we have to choose a particular axis \hat{z} to define \bar{z} or as the surface normal, and in this case we are only sensitive to four of the six TRI face indices, defining whether WCCs (or surface states) zigzag or not along the four edges of the quarter 2D BZ. This determines the strong index ν_0 and two of the three weak indices (ν_1 and ν_2); the procedure has to be repeated with a different choice of axis to obtain the third weak index ν_3 .

In summary, we expect that the flow and connectedness of the WCC sheets and the surface energy bands should always show the same qualitative features. Not surprisingly, similar considerations apply to the case of crystalline TIs as well. Numerous examples will be presented in the following which amply illustrate this bulk-boundary correspondence between the WCC sheets and surface energy bands.

III. MODELS AND CALCULATIONS

We study the properties of WCCs in different topological phases using simple tight-binding (TB) models as well as realistic density-functional theory (DFT) descriptions of known materials. In particular, we use a Haldane-type [36]

TB model of spinless electrons on a hexagonal lattice to study the properties of the WCC sheets in a 3D Chern insulator; the model of Fu, Kane, and Mele (FKM) [4] to study the WCCs of trivial, weak, and strong topological phases; and the tetragonal TB model of Fu [6] to study a crystalline TI. These TB models are described in Sec. III A. We then compute the behavior of the WCC sheets in the Z_2 -even Sb_2Se_3 , weak Z_2 -odd KHgSb , and strong Z_2 -odd Bi_2Se_3 insulators using first-principles DFT calculations. These materials and their crystal structure are described in Sec. III B, and the details of our computational approach are presented in Sec. III C.

A. Tight-binding models

A TB model of a 2D Chern insulator was first introduced by Haldane on a honeycomb lattice [36]. This spinless model is constructed by starting with real first- and second-neighbor hoppings, but the time-reversal symmetry is then broken by introducing local magnetic fluxes in a pattern that respects the symmetry of the lattice and sums to zero in each unit cell. This magnetic flux has the effect of multiplying the second-neighbor hoppings by a unimodular phase factor $\lambda = e^{i\varphi}$. We then stack these 2D layers in the normal direction to make a 3D TB model of a Chern insulator:

$$H = t_1 \sum_{l, \langle ij \rangle} c_{il}^\dagger c_{jl} + t_2 \sum_{l, \langle\langle ij \rangle\rangle} \lambda c_{il}^\dagger c_{jl} + t'_1 \sum_{li} c_{il}^\dagger c_{i,l+1} + t'_2 \sum_{l, \langle ij \rangle} c_{il}^\dagger c_{j,l+1} + \text{H.c.} \quad (7)$$

Here, l is the layer index, single and double brackets label first- and second-neighbor in-plane pairs with hoppings t_1 and t_2 , respectively, and t'_1 and t'_2 are (real) vertical and nearest-diagonal interlayer hoppings, respectively. The hoppings included explicitly in the second term of Eq. (7) are those for clockwise hoppings around the hexagon; counterclockwise ones are accounted for by the Hermitian conjugation and have phases λ^* . With $t_1 = -1.0$, $t'_1 = -0.45$, $t_2 = 0.15$, $t'_2 = 0.015$, and $\varphi = 0.5\pi$, the occupied band has a Chern number of one.

The FKM model [4] is a four-band TB model of s states on a diamond lattice in 3D with a spin-orbit interaction, and takes the form

$$H = t \sum_{\langle ij \rangle} c_i^\dagger c_j + i(8\lambda_{\text{so}}/a^2) \sum_{\langle\langle ij \rangle\rangle} c_i^\dagger \mathbf{s} \cdot (\mathbf{d}_{ij}^1 \times \mathbf{d}_{ij}^2) c_j. \quad (8)$$

Here, the first and second terms describe spin-independent first-neighbor and spin-dependent second-neighbor hoppings, respectively; λ_{so} is the spin-orbit strength, and a is the cubic lattice constant, which is set to one. The second-neighbor hopping between sites i and j depends on spin and on the unit vectors $\mathbf{d}_{ij}^{1,2}$ describing the two first-neighbor bonds that make up the second-neighbor hop. For $t = 1$ and $\lambda_{\text{so}} = 0.125$, the model has a gap closure at the high-symmetry X point in the Brillouin zone.

By varying the relative strength of the nearest-neighbor bond in the $[111]$ direction, $t_{111} = t(1 + \alpha)$, the cubic symmetry is broken and the system can be switched between trivial, weak, and strong topological phases, as shown in Table I. These insulating phases are separated from each other by gap closures at $\alpha = -4, -2, 0$, and 2 . For $\alpha < -4$ and $\alpha > 2$,

TABLE I. Topological phase of the FKM model [4] as a function of parameter α specifying the relative strength of the $[111]$ bond according to $t_{111} = t(1 + \alpha)$.

α	$[\nu_0; \nu_1 \nu_2 \nu_3]$	Topological phase
$(-\infty, -4)$	$[+; + + +]$	Trivial insulator
$(-4, -2)$	$[-; - - -]$	Strong topological insulator
$(-2, 0)$	$[+; + + -]$	Weak topological insulator
$(0, 2)$	$[-; + + -]$	Strong topological insulator
$(2, \infty)$	$[+; + + +]$	Trivial insulator

the t_{111} bond is stronger than the other bonds and the system can be adiabatically transformed to a system of dimers, which is topologically equivalent to a trivial atomic insulator. For $-2 < \alpha < 0$, on the other hand, the t_{111} bond is weaker than the others, and the system can be considered as a collection of 2D spin-Hall layers stacked along the $[111]$ direction. Thus, the system is a weak TI in this range of α . For $-4 < \alpha < -2$ and $0 < \alpha < 2$, t_{111} is stronger than the other first-neighbor bonds, but not strong enough to push the system into the topologically trivial phase. As a result, the 3D KM model is a strong Z_2 TI for these values of α .

For studying the WCC sheet behavior in a topological crystalline insulator, we adopted the TB model of Fu [6], consisting of a tetragonal lattice with two inequivalent A and B atoms stacked above one another, each carrying p_x and p_y orbitals, forming bilayers that we index by n . The total system Hamiltonian can be written as

$$H = \sum_n (H_n^A + H_n^B + H_n^{AB}), \quad (9)$$

where H^A and H^B are the contributions describing intralayer hoppings while H^{AB} describes interlayer ones. The former are given by

$$H_n^X = \sum_{ij} t^X(\mathbf{r}_i - \mathbf{r}_j) \sum_{\alpha, \beta} c_{X\alpha}^\dagger(\mathbf{r}_i, n) e_\alpha^{ij} e_\beta^{ij} c_{X\beta}(\mathbf{r}_i, n) \quad (10)$$

and the latter by

$$H_n^{AB} = \sum_{ij} t'(\mathbf{r}_i - \mathbf{r}_j) \sum_{\alpha, \beta} [c_{A\alpha}^\dagger(\mathbf{r}_i, n) c_{B\beta}(\mathbf{r}_i, n) + \text{H.c.}] + t'_z \sum_i \sum_\alpha [c_{A\alpha}^\dagger(\mathbf{r}_i, n) c_{B\alpha}(\mathbf{r}_i, n_1) + \text{H.c.}] \quad (11)$$

Here, $\mathbf{r} = (x, y)$ labels the coordinate in the plane, $X = \{A, B\}$ labels the sublattice, α and β label the $\{p_x, p_y\}$ orbitals, and e_α^{ij} is cosine of the angle between the bond $(\mathbf{r}_i - \mathbf{r}_j)$ and orbital p_α . We choose the nearest- and next-nearest-neighbor hopping amplitudes to be $t_1^A = -t_1^B = 1$ and $t_2^A = -t_2^B = 0.5$ in H^A and H^B , and $t'_z = 2$, $t'_1 = 2.5$, and $t'_2 = 0.5$ in H^{AB} .

Note that this TB model is spinless, as the spin-orbit coupling plays no role in the nontrivial topology of crystalline TIs. Instead, the topological classification is based on certain crystal point-group symmetries and TRI, leading to robust surface states on those surfaces that respect the symmetries in question. In the tetragonal Fu model, these topological surface states exist on the (001) surface, where the fourfold C_4 rotational symmetry of the crystal is preserved.

B. Material systems

We carry out first-principles calculations of the WCC sheet structure for Sb_2Se_3 , KHgSb , and Bi_2Se_3 as prototypical realizations of trivial, weak, and strong topological phases, respectively. Bi_2Se_3 has a rhombohedral layered structure with space group $D_{3d}^5(R\bar{3}m)$. It consists of quintuple layers (QLs) formed by stacking Se and Bi triangular-lattice planes in the order Se-Bi-Se-Bi-Se, with two identical Bi atoms, two identical Se atoms, and a third Se atom at the center. These QLs have strong internal covalent bonding, but the interaction between QLs is much weaker, being largely of van der Waals type. The states near the Fermi energy come from the Bi $6p$ and Se $4p$ orbitals. The strong spin-orbit coupling (SOC) leads to a band inversion at the Γ point and makes this material a strong Z_2 insulator with a band gap of 0.3 eV [14,37]. Sb_2Se_3 shares the same rhombohedral layered structure as Bi_2Se_3 , but the weaker SOC in this material leaves it in a topological trivial phase.

KHgSb consists of layers of HgSb in a honeycomb lattice, with hexagonal layers of K atoms stuffed between them. In a single layer of KHgSb , the valence bands near the Fermi energy are composed of the Hg $6s$ and Sb $5s$ and $5p$ states, while the K $4s$ band is considerably higher in energy. The strong SOC in the honeycomb HgSb layer leads to a band inversion at the Γ point in the 2D BZ and makes an isolated KHgSb layer a 2D TI. These 2D TI layers can be stacked along the z direction to form a 3D lattice, but the interlayer coupling is very weak and there is little dispersion along the Γ - Z direction. These honeycomb layers can either be stacked in an AA sequence to make a “single-layer” form, or in an $ABAB$ sequence to make a “double-layer” form, where B is rotated by 60° with respect to A . In the latter structure, which is experimentally observed, the primitive cell contains two honeycomb layers. Thus, two band inversions occur and cancel each other out at Γ , and the same happens at Z , making the compound a trivial insulator [38,39]. In the hypothetical single-layered structure, which is proposed as an example of a weak TI [39], there is only one honeycomb layer in the primitive cell, and a single band inversion happens at Γ and another at Z . Thus, single-layered KHgSb can be viewed as a stack of weakly coupled 2D TIs and belongs to the weak Z_2 -odd topological class. Here, we focus on single-layered KHgSb , and we compare its WCC sheets to the weak topological phase of the FKM TB model in Sec. IV C.

C. Computational methods

Our first-principles calculations of WCC sheets are based on DFT calculations using the Perdew-Burke-Ernzerhof (PBE) exchange-correlation functional [40] performed with the QUANTUM ESPRESSO package [41]. We use fully relativistic optimized norm-conserving pseudopotentials from the OPIUM package, with the semicore Bi $5d$, Sb $4d$, Hg $5d$, and K $3s3p$ states included in the valence. The self-consistent calculations are carried out for the experimental structures using a $10 \times 10 \times 10$ Monkhorst-Pack [42] k mesh. The plane-wave energy cutoff is set to 70 Ry.

In principle, one could include all occupied bands in the WCC construction. However, taking Bi_2Se_3 as an example, the occupied Bi $5d$ semicore states and the shallow Bi $6s$ and

Se $4s$ bands have an obvious atomic character and remain well separated from the active valence p bands, so they are clearly trivial and do not need to be included in the topological analysis. Therefore, we concentrate on constructing WCC sheets only for the remaining upper valence bands. As these are the lowest 18 of the 30 bands of Bi $6p$ and Se $4p$ character, we do this by constructing a Wannier representation in this 30-band space using the WANNIER90 package [43] to generate an *ab initio* TB Hamiltonian from the DFT calculation. The frozen window in which the first-principles band structure is exactly reproduced extends from 2 eV below to 2 eV above the Fermi level E_F . From the outer energy window, which extends to 20 eV above E_F , 80 Bloch bands are used to produce 30 WFs for the Bi, Sb, and Se p bands in Bi_2Se_3 and Sb_2Se_3 . The orbital positions and hopping parameters between them are then used to construct the effective tight-binding Hamiltonians. Similarly, for KHgSb we carry out the Wannier construction for the 10 Bloch bands of K $4s$, Hg $6s$, and Sb $5p$ character, of which the bottom six are the highest valence states. The outer window is chosen at 14 eV above E_F for KHgSb , with 10 WFs constructed from 20 Bloch bands.

We have implemented the calculation of the WCC sheets into Version 1.6.2 of the open-source PYTHTB tight-binding code package [44]. The Wannierized Hamiltonians are imported into the PYTHTB code to calculate the WCC sheets using the parallel-transport approach explained in Sec. II A.

IV. RESULTS

In this section, we present the WCC sheets for the different topological phases we have studied. For the 3D Chern insulator in Sec. IV A, the WCC sheets are plotted over the entire 2D BZ, while for the TR-invariant systems of Secs. IV B–IV D, the sheets are plotted over one quarter of the BZ, i.e., between the TRI momenta $[0,0]$, $[0,\pi]$, $[\pi,\pi]$, and $[\pi,0]$.

The axis of highest rotational symmetry in each TB model or material system is chosen as the z axis. This axis in the FKM model is along the bond with altered strength (t_{111}); the model has a threefold symmetry around this axis, which when combined with TR symmetry results in a sixfold-rotational symmetry in the 2D BZ. In Sb_2Se_3 and Bi_2Se_3 , the z axis is normal to the quintuple layers, which is the axis of threefold symmetry. In KHgSb , the z axis is chosen normal to the honeycomb HgSb layers, and in the Fu tetragonal TB model it is along the tetragonal axis.

The WCC sheets are computed along both z and y and plotted versus (k_x, k_y) and (k_x, k_z) , respectively. (Henceforth, we shall not be careful about the distinction between k_x and $\tilde{k}_x = k_x a$, etc.; the meaning should be clear from the context.) Plotting the WCC sheets along these two perpendicular directions is especially important to reveal the topological behavior in the 3D Chern, weak Z_2 , and topological crystalline phases, where, as we shall see, the topology of the WCC sheets may look trivial in one direction but topological in another.

The WCC sheets for the TR-broken Chern insulator phase are discussed next. WCC sheets for the TR-invariant trivial, weak, and strong Z_2 phases are discussed in Secs. IV B–IV D, using the FKM model and its material system analogs in each phase. The WCC sheets for the crystalline topological phase are discussed in Sec. IV E.

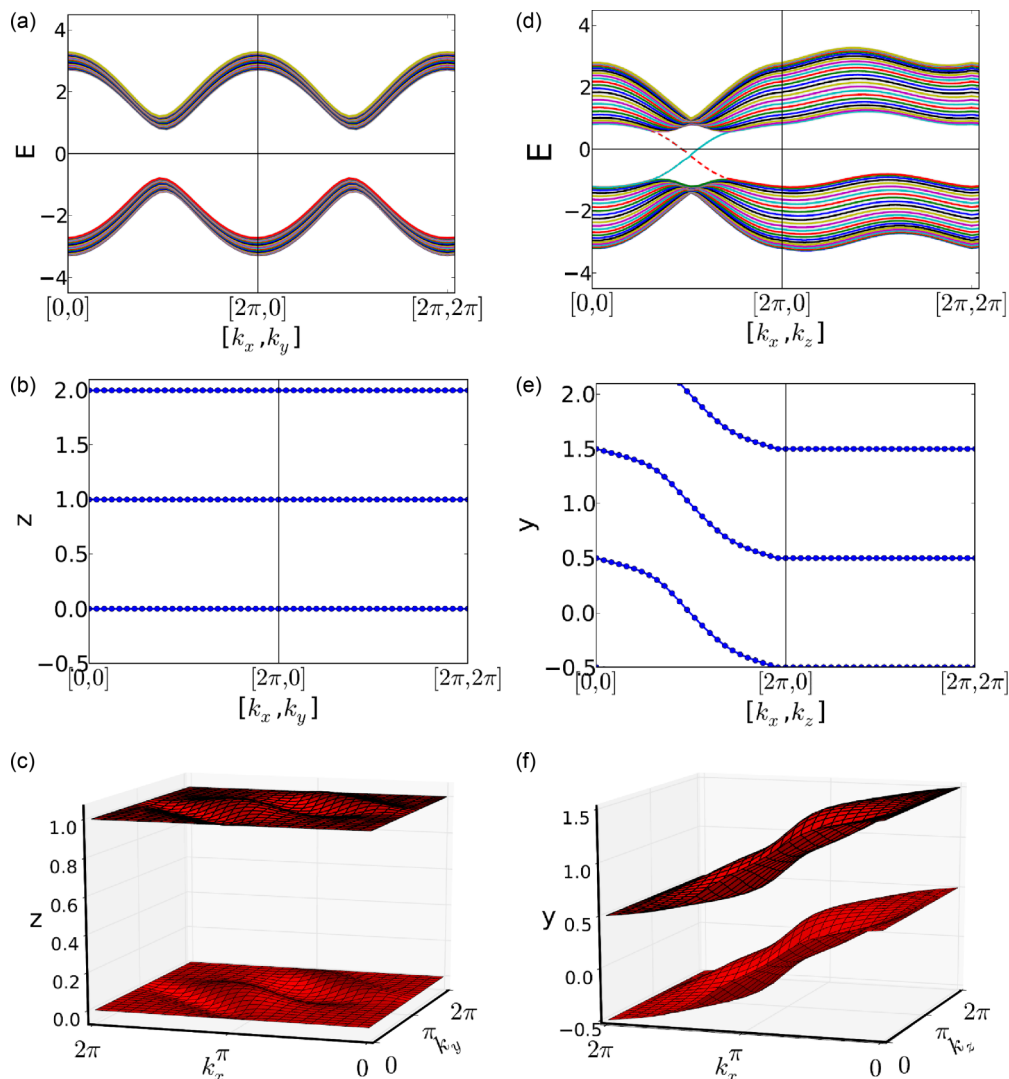


FIG. 2. (Color online) Surface energy bands and WCC sheets for the TR-broken Chern insulator model. (a)–(c) Surface normal and WCCs along \hat{z} vs (k_x, k_y) . (d)–(f) Surface normal and WCCs along \hat{y} vs (k_x, k_z) . Surface states for a 24-layer slab in (a) and (d); WCCs around 2D BZ boundary in (b) and (e); WCCs in 2D BZ in (c) and (f). Dashed and solid surface states in (d) reside on the top and bottom of the (010) slab, respectively. The WCC sheets and surface bands wind by one unit in the k_y - k_z plane, but not in the k_x - k_y plane.

A. TR-broken Chern insulator

We first consider the TB model for a TR-broken Chern insulator phase that was introduced in Sec. III A. It is composed of 2D Chern layers stacked along the z direction with weak interlayer coupling, so we do not expect an (001) slab of the 3D model to show any topological surface states. This is confirmed in the surface projected band structure plotted in Fig. 2(a), where the shaded region indicates the region of bulk energy bands. No surface states are visible in this case, consistent with the trivial topology for this orientation. By the same token, the WCC sheets computed along the z direction from the single occupied band remain localized in the vicinity of the z positions of the layers, with no topological evolution along k_x or k_y . This is shown in Figs. 2(b) and 2(c), where the WCC sheets are plotted around the boundary, and throughout the interior, of the 2D projected BZ, respectively.

In contrast, any slab of the 3D system that cuts through the 2D Chern layers will reveal the topological nature of the

3D crystal by displaying a surface energy band traversing the bulk gap on each surface, as shown in Fig. 2(d) for a (010) slab. The corresponding $\bar{y}(k_x, k_z)$ WCC sheets are shown in Figs. 2(e)–2(f). While these WCCs do not vary strongly along k_z , they wind by one unit as they evolve along k_x , pumping one electron per unit cell from the $(0\bar{1}0)$ to the (010) surface. The pumped charge is restored on each surface as the surface bands cross the Fermi level in the bulk energy gap.

B. TR-invariant trivial insulator

In general, the broken translational symmetry at the surface of a band insulator allows for the existence of surface states in the bulk band gap. In a topologically trivial insulator, these surface states, if present, are prone to localization by disorder and can be removed from the gap by an adiabatic transformation of the Hamiltonian. An example of such unprotected surface states can be seen in Fig. 3(a), which shows the surface

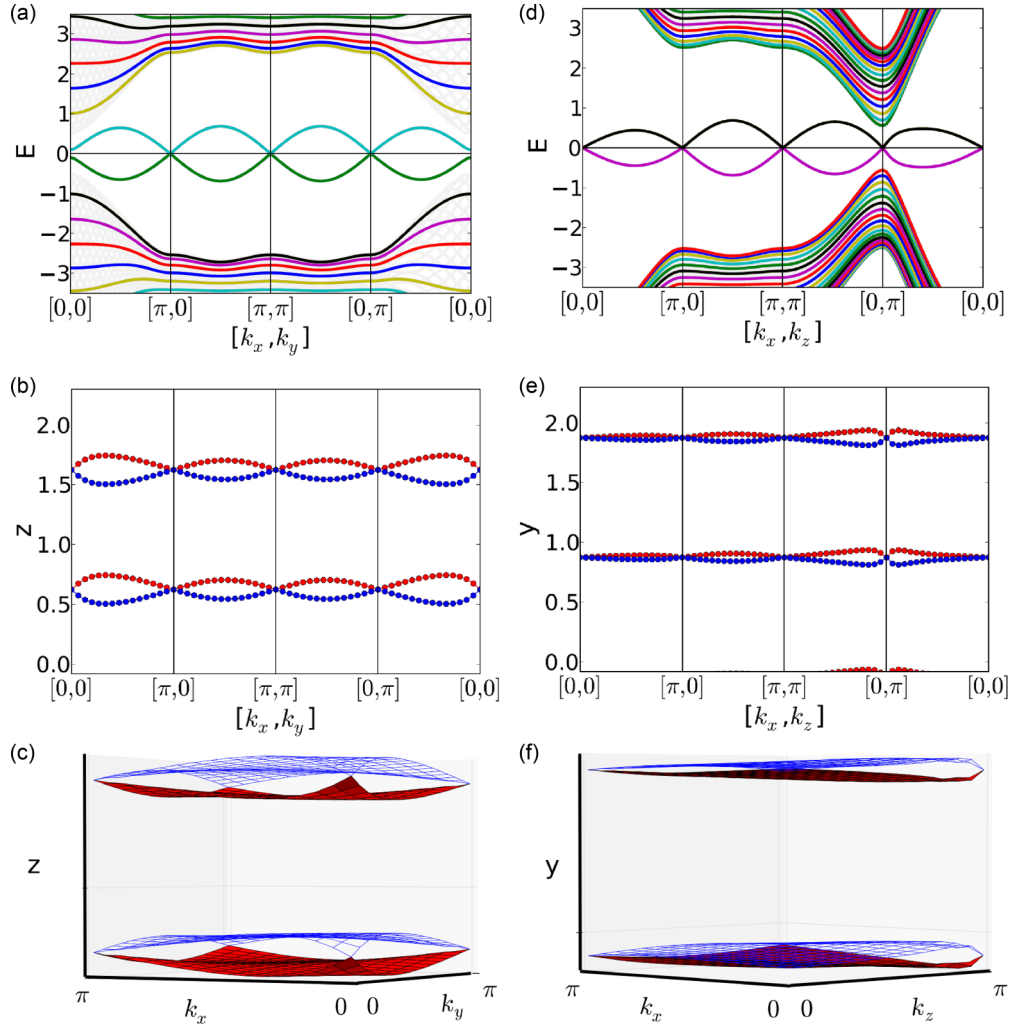


FIG. 3. (Color online) Surface energy bands (15-layer slab) and WCC sheets for the TR-invariant FKM model in the trivial phase ($\alpha = 2.5$). (a)–(c) Surface normal and WCCs along \hat{z} vs (k_x, k_y) . (d)–(f) Surface normal and WCCs along \hat{y} vs (k_x, k_z) . The WCC sheets and surface bands show a trivial behavior in all directions.

states on the (001) surface of the FKM model in its trivial insulating phase. The surface bands are doubly degenerate at the TRI momenta as required by Kramer's theorem, but nothing protects them from being adiabatically pushed to the valence or conduction band. (The model also happens to have a particle-hole symmetry which is responsible for the mirror symmetry along the energy axis, but we do not consider this as an imposed symmetry here.) The surface energy bands on the (010) surface [Fig. 3(d)] show the same trivial behavior, indicating that this is a topologically trivial insulator.

The trivial topology of this material is equally evident from the WCC sheets, plotted along \hat{z} and \hat{y} in Figs. 3(b) and 3(c) and 3(e) and 3(f), respectively. The WCC sheets are plotted around the boundary of a quadrant of the 2D projected BZ in Figs. 3(b) and 3(e), and throughout its interior in Figs. 3(c) and 3(f). Here, there are two WCC sheets per unit cell (vertical axis) because there are two occupied energy bands in the four-band model, but the band pairs remain well separated from their periodic images above and below. The WCC sheets touch at the TRI points at the corners of the quarter BZ, as required by Kramer's theorem, but these Kramer pairs are connected

in all directions in a topologically trivial way. As a result, the topological index is $\nu_\mu = +1$ on all six TRI faces, signaling a fully trivial topological phase.

A similar trivial behavior is seen in the first-principles WCCs computed for Sb_2Se_3 as shown in Fig. 4. The 18 WCC sheets in the quintuple layer come mainly from the Sb 5*p* and Se 4*p* orbitals. While having substantial Sb 5*p* character, they are nevertheless centered on the anion Se sites located at $z \simeq -0.3c, 0$, and $0.3c$ in the figure. While the gap between WCC sheets associated with neighboring quintuple layers, centered at $0.5c$ in Fig. 4(a), is not obviously larger than the other gaps, it nevertheless remains open across the entire 2D BZ. The WCC sheets plotted along the *x* and *y* directions (not shown) display a similar trivial behavior. Thus, we can conclude that this is a fully trivial insulator, without having to carry out any surface-state calculation.

C. TR-invariant weak topological insulator

The FKM model with $-2 \leq \alpha \leq 0$ is a weak Z_2 -odd insulator, as illustrated by our results for $\alpha = -1$ in Fig. 5. In this case, the crystal can be thought of as a series of 2D

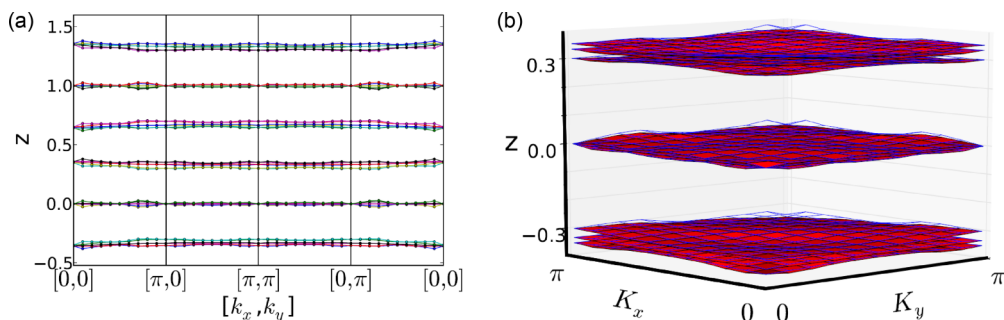


FIG. 4. (Color online) First-principles WCC sheets along \hat{z} for topologically trivial Sb_2Se_3 , plotted on (a) the boundary and (b) the interior of the 2D quarter BZ. The WCCs show trivial behavior as expected.

spin-Hall insulators stacked along the z direction, i.e., the direction of the weakest bond. Thus, a slab of the model cut normal to this direction shows no robust surface states in the bulk energy gap, as shown in Fig. 5(a), and the WCC sheets along this direction pair up as they do in a trivial insulator, as can be seen in Figs. 5(b) and 5(c).

On the other hand, a slab of a weak Z_2 -odd insulator cut through the 2D spin-Hall sheets should host an even

number of Dirac cones on each surface. These surface states are shown for an (010) slab of the same FKM model in Fig. 5(d), where the Dirac cones are visible at $(k_x, k_z) = (0, 0)$ and $(0, \pi)$. These surface bands have a gap-crossing Z_2 -odd behavior versus k_x but not versus k_z , suggesting that the (k_x, k_y) TRI faces of the 3D BZ are Z_2 odd at $k_z = 0$ and π , while those on the (k_y, k_z) faces are Z_2 even at $k_x = 0$ and π . This is confirmed in Figs. 5(e) and 5(f), where the

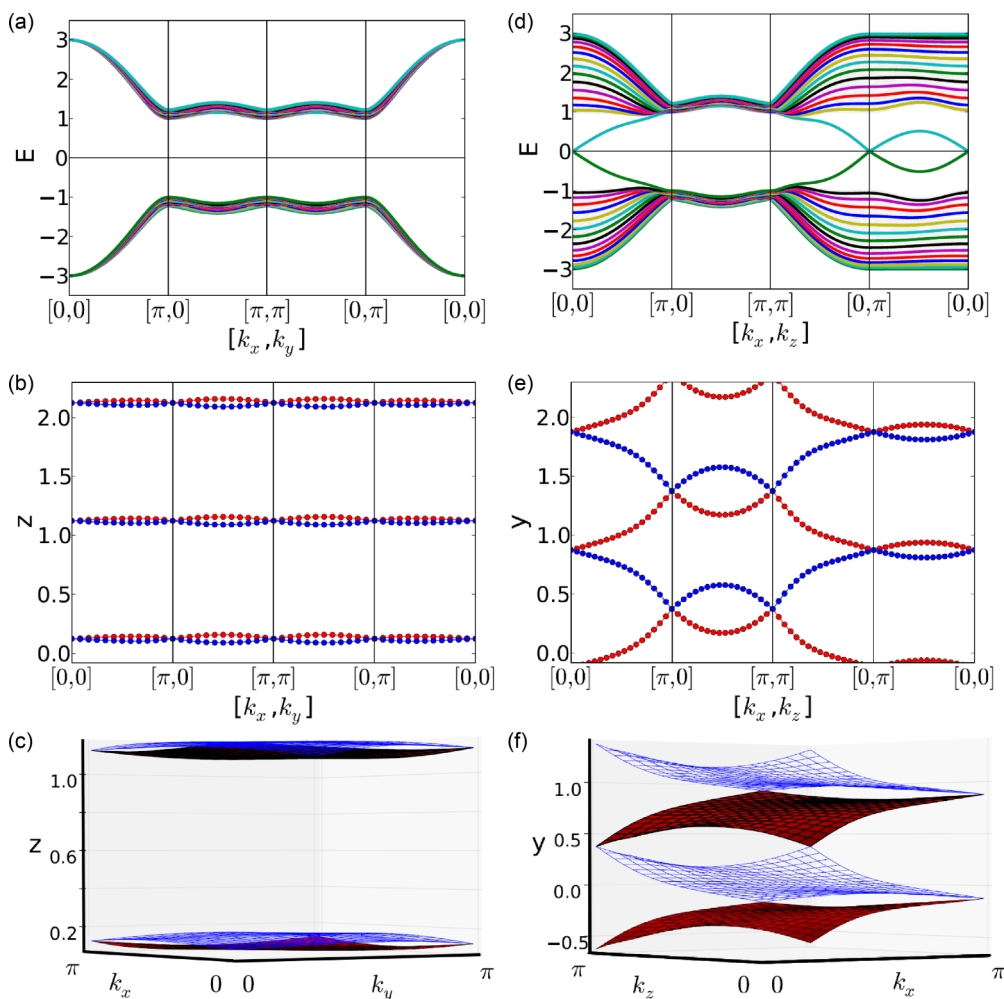


FIG. 5. (Color online) Surface energy bands (15-layer slab) and WCC sheets for the TR-invariant FKM model in the weak topological phase ($\alpha = -1$). (a)–(c) Surface normal and WCCs along \hat{z} vs (k_x, k_y) . (d)–(f) Surface normal and WCCs along \hat{y} vs (k_x, k_z) . Only the (k_x, k_y) TRI faces at $k_z = 0$ and π are Z_2 odd.

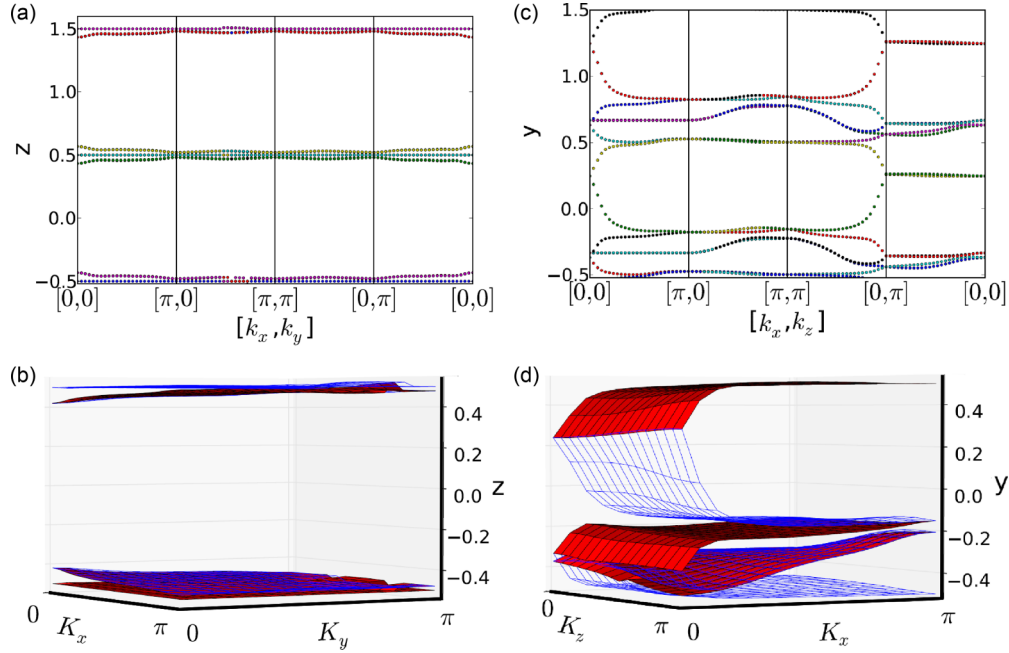


FIG. 6. (Color online) First-principles WCC sheets for the weak TI KHgSb. (a), (b) Along \hat{z} . (c), (d) Along \hat{y} . Only the (k_x, k_y) TRI faces at $k_z = 0$ and π are Z_2 odd.

WCC sheets are seen to swap partners versus k_x but not versus k_z .

The Z_2 topological invariants ν_μ follow straightforwardly from the above considerations. The invariants are $+1$ for the TRI faces at $k_x = 0$ and π , $+1$ for the TRI faces at $k_y = 0$ and π , and -1 for the TRI faces at $k_z = 0$ and π . The conventional index set is then $[\nu_0; \nu_1 \nu_2 \nu_3] = [+; ++ -]$, confirming that this is a weak TI ($\nu_0 = +1$) corresponding to spin-Hall layers stacked along z ($\nu_3 = -1$).

We see the same kind of weak topological behavior in our first-principles calculations of the WCC sheets for KHgSb shown in Fig. 6. As explained in Sec. III B, this material is composed of honeycomb HgSb layers that behave as 2D spin-Hall insulators, stacked along the z direction, and separated by hexagonal layers of K stuffing atoms. The pictures look more complicated because there are now six occupied bands per cell, and thus six WCCs per lattice constant, and some of the artificial symmetries of the FKM model are now absent. However, the topological behavior is similar to that of Fig. 5. The weak coupling between the HgSb layers is reflected in the trivial behavior of the WCC sheets along the (001) direction [Figs. 6(a) and 6(b)], but plotting the WCCs in a direction cutting across the honeycomb HgSb layers reveals the topological behavior, as seen in Figs. 6(c) and 6(d). These WCC sheets change partners on the (k_x, k_y) TRI faces at both $k_z = 0$ and π , indicating $\nu_3 = -1$ and $\nu_0 = +1$, giving the same $[+, ++ -]$ set of indices as for the FKM model in its weak topological phase. These results are entirely consistent with the existence of Dirac cones at the $\bar{\Gamma}$ and \bar{Z} points in the surface bands of an (010) slab as shown in Ref. [39]. However, we again emphasize the convenience of our approach, in which only primitive-cell bulk calculations are needed.

D. TR-invariant strong topological insulator

In contrast to weak TIs, the nontrivial behavior of the WCC sheets in strong Z_2 insulators should be evident no matter what direction is chosen to construct them; there would be switching of partners for one of the TRI faces in any chosen direction. This behavior is illustrated in Fig. 7, where the surface bands and WCC sheets are presented for the FKM model in the strong Z_2 -odd phase at $\alpha = 1$. Both the surface bands and the WCC sheets swap partners in the (k_x, k_y) plane at $k_z = \pi$, the (k_x, k_z) plane at $k_y = 0$, and the (k_y, k_z) plane at $k_x = 0$, but not on the other three TRI faces. The set of topological indices is therefore $[\nu_0; \nu_1 \nu_2 \nu_3] = [-; ++ -]$, and the system is a strong TI. This is also consistent with the existence of an odd number of Dirac cones on any surface of a strong Z_2 insulator, as is evident in Figs. 7(a) and 7(d), where three Dirac cones are visible in each case.

We again confirm that our approach works in the first-principles context by presenting the WCC sheets along the z direction (rhombohedral axis) in the strong TI Bi_2Se_3 , as shown in Fig. 8. There are now 18 WCC sheets per cell; in most of the 2D projected BZ these are clustered in groups of six, with each of the three clusters located close to the z position of a layer of Se atoms within the QL. This is reasonable, as the Bi and Se atoms can be regarded as cations and anions, respectively, and it is natural to find the Wannier centers on the anions. However, this behavior changes drastically near $\bar{\Gamma}$, where two of the six WCC sheets in each cluster split off and form a Dirac point at $\bar{\Gamma}$, signaling the strong TI nature of this material. Clearly, this results from the band inversion near Γ in the 3D bulk BZ, and is consistent with the existence of a single Dirac cone at $\bar{\Gamma}$ on the surface of Bi_2Se_3 , as has been amply demonstrated by angle-resolved photoemission and other experimental probes [19]. We can again read off

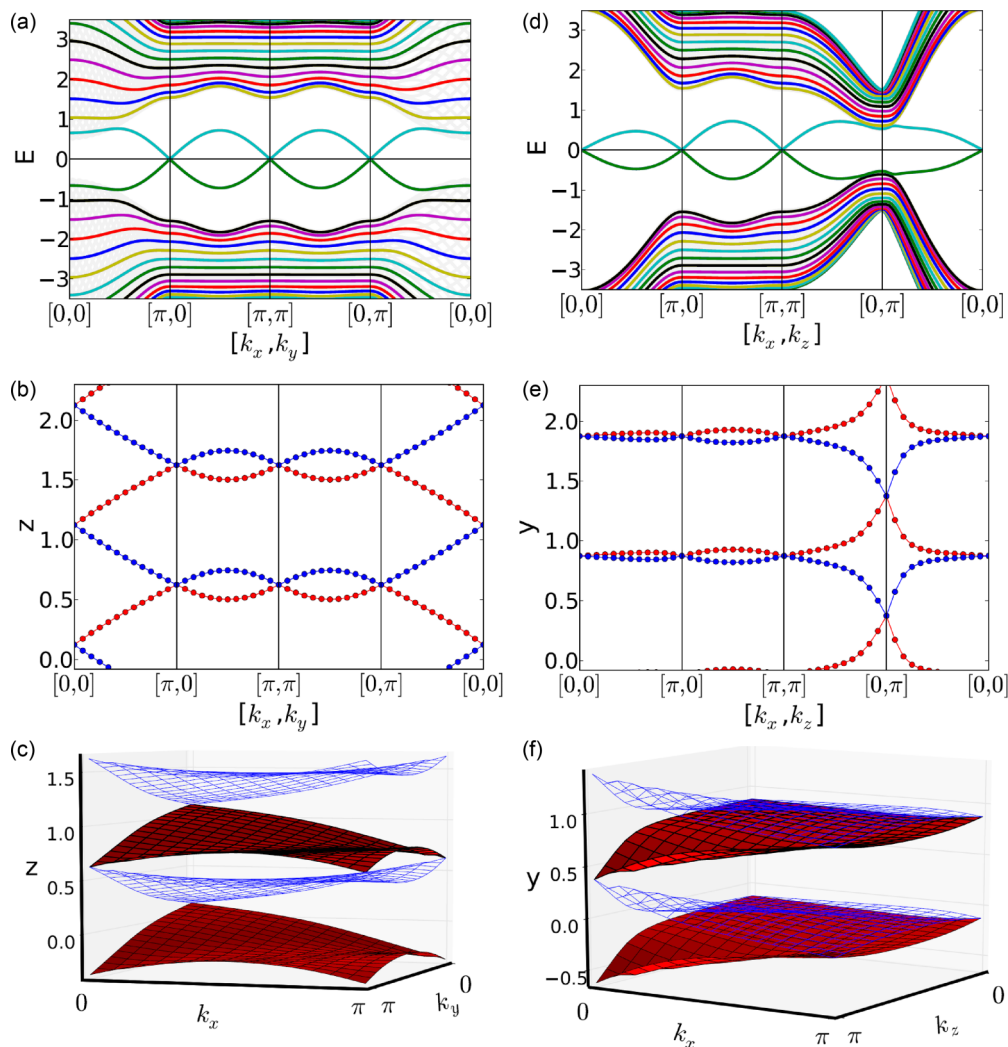


FIG. 7. (Color online) Surface energy bands (15-layer slab) and WCC sheets for the TR-invariant FKM model in the strong topological phase ($\alpha = 1$). (a)–(c) Surface normal and WCCs along \hat{z} vs (k_x, k_y) . (d)–(f) Surface normal and WCCs along \hat{y} vs (k_x, k_z) . The (k_x, k_y) TRI face at $k_z = \pi$, the (k_x, k_z) TRI face at $k_y = 0$, and the (k_y, k_z) TRI face at $k_x = 0$ are Z_2 odd.

the topological indices by noting that the WCC sheets swap partners in the (k_x, k_y) plane at $k_z = 0$, the (k_x, k_z) plane at $k_y = 0$, and the (k_y, k_z) plane at $k_x = 0$, but not on the other three TRI faces, so that $[\nu_0; \nu_1 \nu_2 \nu_3] = [-; ++ +]$.

E. Crystalline topological insulator

In contrast to the systems studied above, Fu's tetragonal model for a crystalline TI [6] is spinless because the nontrivial topology of a topological crystalline insulator has its roots

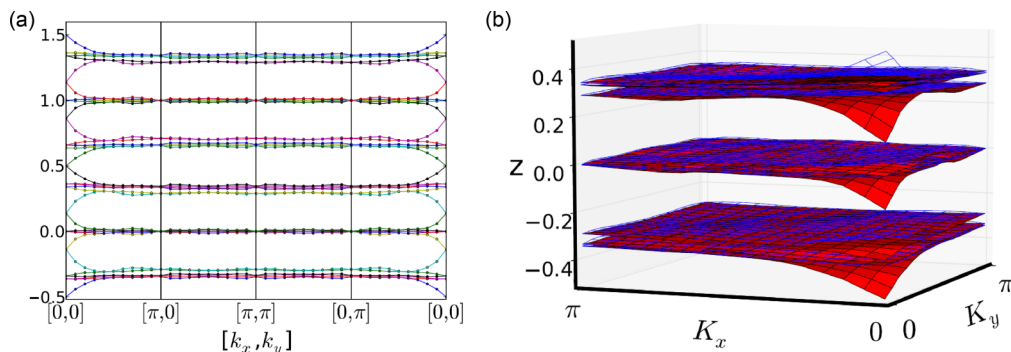


FIG. 8. (Color online) First-principles WCC sheets for the strong TI Bi_2Se_3 , plotted on (a) the boundary and (b) the interior of the 2D quarter BZ. The WCC sheets on parallel TRI faces (e.g., at $k_x = 0$ and π) show opposite topological behavior.

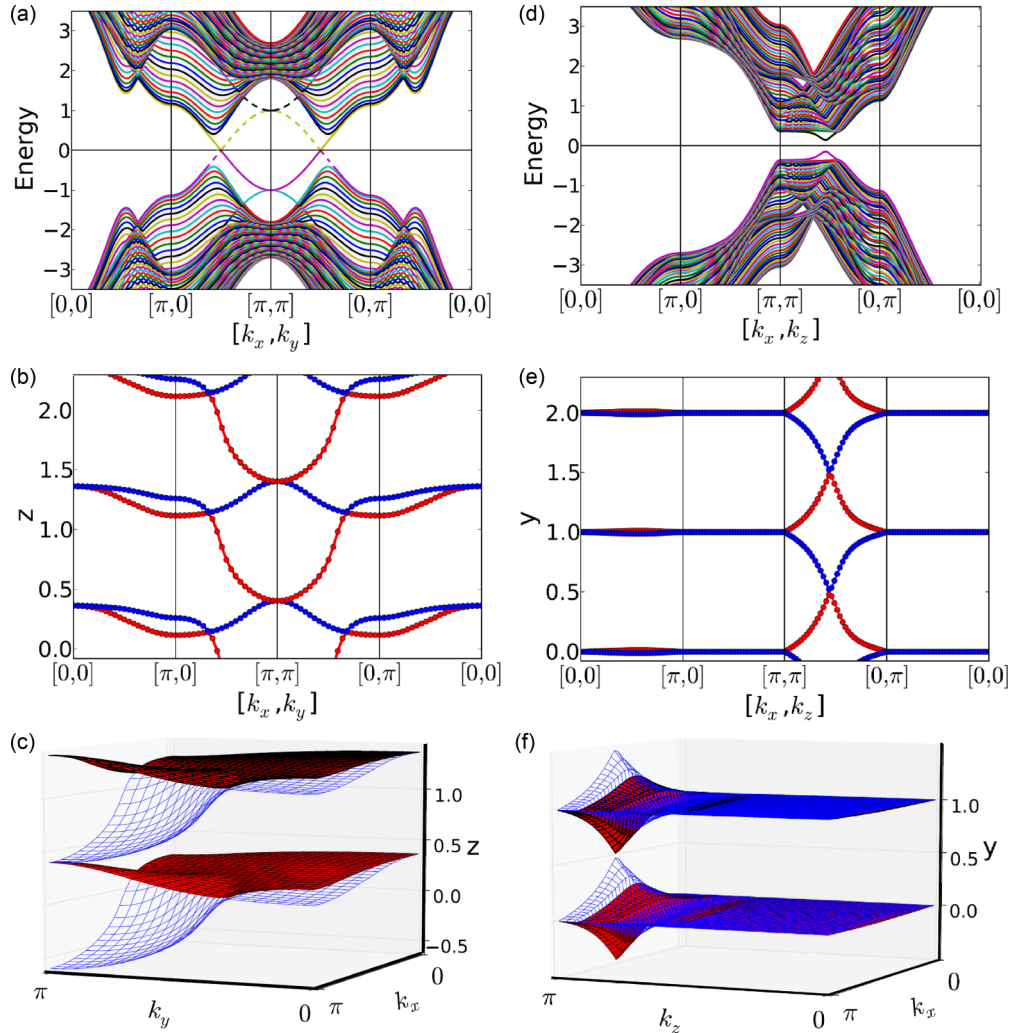


FIG. 9. (Color online) Surface energy bands (24-layer slab) and WCC sheets for tight-binding model of a crystalline TI. (a)–(c) Surface normal and WCCs along \hat{z} vs (k_x, k_y) . (d)–(f) Surface normal and WCCs along \hat{y} vs (k_x, k_z) . Dashed and solid surface states in (a) reside on the top and bottom of the (001) slab, respectively. Quadratic band touching and cross linking in panels (a)–(c) signal the crystalline topological phase.

in the crystal symmetries rather than in TR symmetry and spin-orbit interaction. The TR symmetry in this scalar model does not guarantee double degeneracy at the TRI momenta, but its combination with the crystal C_4 symmetry leads to a twofold degeneracy of the surface energy bands at $\bar{\Gamma} = (0,0)$ and at $\bar{M} = (\pi/a, \pi/a)$ for the (001) surface, where z is chosen along the tetragonal axis. These surface bands can be seen in Fig. 9(a) for an (001) slab of the model. The dashed and solid lines show the surface states on the two surfaces of the slab. These bands traverse the energy gap in a zigzag manner, and their protected degeneracy at the \bar{M} point guarantees a robust metallic (001) surface. This nontrivial behavior is clearer when considering the behavior of the WCC sheets along the z direction, plotted in Figs. 9(b) and 9(c). Over most of the 2D BZ, the z location of these sheets is midway between the A and B atoms. The sheets touch two-by-two at $\bar{\Gamma}$, but they open up and switch partners on approaching the \bar{M} point. Thus, the WCC undergo the same kind of switching, and so reflect the same topological properties, as in the surface energy bands. Even the quadratic dispersion of the surface bands around \bar{M} is reflected in the WCCs.

The C_4 symmetry is broken on any surface other than the (001) surface, which means no robust surface states are expected on these other surfaces. Figure 9(d) confirms this for the case of an (010) slab of the model. The energy bands approach each other near a point midway between $(k_x, k_z) = (\pi, \pi)$ and $(0, \pi)$, but they do not touch. The WCC sheets show a similar behavior in Figs. 9(e) and 9(f), remaining trivial except along the segment at $k_z = \pi$; while there is a nonavoided crossing along this line, this appears to be an artifact of some special symmetries of the model, and is not relevant to the discussion at hand.¹ Thus, both the surface bands and WCC sheets are consistent with the trivial topology of an (010) slab of the model.

¹The topological index for the path from (π, π) to $(0,0)$ (third and fourth panels) in Fig. 9(e) is even because a horizontal segment drawn at any chosen y crosses the sheets an even number of times along this path; this is true regardless of whether the crossing is avoided or not.

V. SUMMARY

In this paper, we have explained how the hybrid Wannier charge centers, or WCC sheets, can be calculated using a parallel-transport approach along a chosen direction in a 3D insulator and plotted versus the other k -space dimensions. We have shown that these sheets contain the same topological information as the surface energy bands, and thus provide an accessible means of deducing the topological invariants of the insulator from the bulk properties alone. We also show that the linear dispersion of the surface energy bands at Dirac points in Z_2 TIs, and their quadratic behavior at the gap closure in topological crystalline insulators, are replicated by the WCCs. Moreover, the symmetry group of the WCCs in the 2D BZ includes all the symmetry operators of the surface bands.

We have demonstrated the distinct behavior of the WCC sheets in trivial, Chern, weak, strong, and crystalline TIs using various tight-binding models. In addition, we have used first-principles calculations to illustrate the calculation of the WCC sheets in Z_2 -even Sb_2Se_3 , weak Z_2 -odd KHgSb , and strong Z_2 -odd Bi_2Se_3 , confirming the conclusions from the tight-binding models.

Admittedly, the topological invariants of Chern, TR-invariant, and crystalline TIs can be deduced in other ways. For example, for the TR-invariant case, parity eigenvalues can be used if inversion symmetry is present; if not, a calculation of 1D Wannier centers on each 2D TRI face is sufficient [22,23].

However, the WCC sheets provide a unifying description that works in all these cases, allows for a more intuitive comparison of different kinds of TIs, and provides deeper insight into the origins of the nontrivial topology.

The evolution of the WCC sheets as the Hamiltonian is varied through a trivial-to-topological phase transition, or carried adiabatically around a loop that pumps the Chern-Simons axion coupling by a quantum [45,46], would be interesting targets for future studies. Other phases, such as axion insulators [47] and antiferromagnetic TIs [48], might also be good subjects for investigation with this tool. Even in zero-gap Weyl semimetals, the WCC sheets will be well defined everywhere except at isolated projected Weyl points in the 2D BZ, and studying their distinct topological properties would be interesting. Finally, it would be intriguing to explore whether the WCC concept can be generalized to topological superconductors. Thus, we are hopeful that the construction and inspection of the Wannier charge center sheets will prove to be a useful tool for the characterization of topological matter in general.

ACKNOWLEDGMENT

This work was supported by NSF Grant No. DMR-10-05838.

-
- [1] D. J. Thouless, M. Kohmoto, M. P. Nightingale, and M. den Nijs, *Phys. Rev. Lett.* **49**, 405 (1982).
 - [2] C. L. Kane and E. J. Mele, *Phys. Rev. Lett.* **95**, 146802 (2005).
 - [3] C. L. Kane and E. J. Mele, *Phys. Rev. Lett.* **95**, 226801 (2005).
 - [4] L. Fu, C. L. Kane, and E. J. Mele, *Phys. Rev. Lett.* **98**, 106803 (2007).
 - [5] J. E. Moore and L. Balents, *Phys. Rev. B* **75**, 121306 (2007).
 - [6] L. Fu, *Phys. Rev. Lett.* **106**, 106802 (2011).
 - [7] Y. Hatsugai, *Phys. Rev. Lett.* **71**, 3697 (1993).
 - [8] X. L. Qi, Y. S. Wu, and S. C. Zhang, *Phys. Rev. B* **74**, 045125 (2006).
 - [9] G. Graf and M. Porta, *Commun. Math. Phys.* **324**, 851 (2013).
 - [10] J. C. Avila, H. Schulz-Baldes, and C. Villegas-Blas, *Math. Phys., Anal. Geom.* **16**, 137 (2013).
 - [11] A. M. Essin and V. Gurarie, *Phys. Rev. B* **84**, 125132 (2011).
 - [12] Y. L. Chen, J. G. Analytis, J. Chu, Z. K. Liu, S. Mo, X. L. Qi, H. J. Zhang, D. H. Lu, X. Dai, Z. Fang *et al.*, *Science* **325**, 178 (2009).
 - [13] D. Hsieh, D. Qian, Y. X. L. Wray, Y. S. Hor, R. J. Cava, and M. Z. Hasan, *Nature (London)* **452**, 970 (2008).
 - [14] Y. Xia, D. Qian, D. Hsieh, L. Wray, A. Pal, A. B. H. Lin, D. Grauer, Y. S. Hor, R. J. Cava, and M. Z. Hasan, *Nat. Phys.* **5**, 398 (2009).
 - [15] J. G. Analytis, J.-H. Chu, Y. Chen, F. Corredor, R. D. McDonald, Z. X. Shen, and I. R. Fisher, *Phys. Rev. B* **81**, 205407 (2010).
 - [16] D. Hsieh, D. Q. Y. Xia, L. Wray, F. Meier, J. H. Dil, J. O. L. Patthey, A. V. Fedorov, H. Lin, A. Bansil, D. Grauer *et al.*, *Phys. Rev. Lett.* **103**, 146401 (2009).
 - [17] S. R. Park, W. S. Jung, C. Kim, D. J. Song, C. Kim, S. Kimura, K. D. Lee, and N. Hur, *Phys. Rev. B* **81**, 041405 (2010).
 - [18] H. Lin, L. A. Wray, Y. Xia, S. Xu, S. Jia, R. J. Cava, A. Bansil, and M. Z. Hasan, *Nat. Mater.* **9**, 546 (2010).
 - [19] M. Z. Hasan and C. L. Kane, *Rev. Mod. Phys.* **82**, 3045 (2010).
 - [20] T. Fukui and Y. Hatsugai, *J. Phys. Soc. Jpn.* **76**, 053702 (2007).
 - [21] I. C. Fulga, F. Hassler, and A. R. Akhmerov, *Phys. Rev. B* **85**, 165409 (2012).
 - [22] A. A. Soluyanov and D. Vanderbilt, *Phys. Rev. B* **83**, 235401 (2011).
 - [23] R. Yu, X. L. Qi, A. Bernevig, Z. Fang, and X. Dai, *Phys. Rev. B* **84**, 075119 (2011).
 - [24] T. Fukui, Y. Hatsugai, and H. Suzuki, *J. Phys. Soc. Jpn.* **74**, 1674 (2005).
 - [25] E. Prodan, *Phys. Rev. B* **83**, 235115 (2011).
 - [26] L. Fu and C. L. Kane, *Phys. Rev. B* **74**, 195312 (2006).
 - [27] A. Alexandradinata, Xi Dai, and B. Andrei Bernevig, [arXiv:1208.4234](https://arxiv.org/abs/1208.4234).
 - [28] N. Marzari and D. Vanderbilt, *Phys. Rev. B* **56**, 12847 (1997).
 - [29] D. J. Thouless, *J. Phys. C: Solid State Phys.* **17**, L325 (1984).
 - [30] T. Thonhauser and D. Vanderbilt, *Phys. Rev. B* **74**, 235111 (2006).
 - [31] A. A. Soluyanov and D. Vanderbilt, *Phys. Rev. B* **83**, 035108 (2011).
 - [32] C. Sgariello, M. Peressi, and R. Resta, *Phys. Rev. B* **64**, 115202 (2001).
 - [33] S. Coh and D. Vanderbilt, *Phys. Rev. Lett.* **102**, 107603 (2009).
 - [34] X. Wu, O. Diéguez, K. M. Rabe, and D. Vanderbilt, *Phys. Rev. Lett.* **97**, 107602 (2006).

- [35] Y. Yao and H. Fu, *Phys. Rev. B* **79**, 014103 (2009).
- [36] F. D. M. Haldane, *Phys. Rev. Lett.* **61**, 2015 (1988).
- [37] G. Zhang, H. Qin, J. Teng, J. Guo, Q. Guo, X. Dai, Z. Fang, and K. Wua, *Appl. Phys. Lett.* **95**, 053114 (2009).
- [38] H.-J. Zhang, S. Chadov, L. Muchler, B. Yan, X.-L. Qi, J. Kubler, S.-C. Zhang, and C. Felser, *Phys. Rev. Lett.* **106**, 156402 (2011).
- [39] B. Yan, L. Muchler, and C. Felser, *Phys. Rev. Lett.* **109**, 116406 (2012).
- [40] J. P. Perdew, K. Burke, and M. Ernzerhof, *Phys. Rev. Lett.* **77**, 3865 (1996).
- [41] P. Giannozzi, S. Baroni, N. Bonini, M. Calandra, R. Car, C. Cavazzoni, D. Ceresoli, G. L. Chiarotti, M. Cococcioni, I. Dabo *et al.*, *J. Phys.: Condens. Matter* **21**, 395502 (2009).
- [42] H. J. Monkhorst and J. D. Pack, *Phys. Rev. B* **13**, 5188 (1976).
- [43] A. A. Mostofi, J. R. Yates, Y.-S. Lee, I. Souza, D. Vanderbilt, and N. Marzari, *Comput. Phys. Commun.* **178**, 685 (2008).
- [44] Available at <http://www.physics.rutgers.edu/pythtb/index.html>
- [45] X.-L. Qi, T. L. Hughes, and S.-C. Zhang, *Phys. Rev. B* **78**, 195424 (2008).
- [46] A. M. Essin, J. E. Moore, and D. Vanderbilt, *Phys. Rev. Lett.* **102**, 146805 (2009).
- [47] X. Wan, A. Vishwanath, and S. Y. Savrasov, *Phys. Rev. Lett.* **108**, 146601 (2012).
- [48] R. S. K. Mong, A. M. Essin, and J. E. Moore, *Phys. Rev. B* **81**, 245209 (2010).